Sine-square deformation applied to classical Ising models

Chisa Hotta and Takashi Nakamaniwa

Graduate School of Arts and Sciences, University of Tokyo, 3-8-1 Komaba, Meguro-ku, Tokyo 1538902, Japan

Tota Nakamura ●

College of Engineering, Shibaura Institute of Technology, Saitama 337-8570, Japan

Sine-square deformation (SSD) is a treatment proposed in quantum systems, which spatially modifies a Hamiltonian, gradually decreasing the local energy scale from the center of the system toward the edges by a sine-squared envelope function. It is known to serve as a good boundary condition as well as to provide physical quantities reproducing those of the infinite-size systems. We apply the SSD to one- and two-dimensional classical Ising models. Based on the analytical calculations and Monte Carlo simulations, we find that the classical SSD system is regarded as an extended canonical ensemble of a local subsystem, each characterized by its own effective temperature. This effective temperature is defined by normalizing the system temperature by the deformed local energy scale. A single calculation for a given system temperature provides a set of physical quantities of various temperatures that quantitatively reproduces well those of the uniform system.

I. INTRODUCTION

The Hamiltonian in condensed matter physics is spatially uniform in most cases, and its symmetry determines the physical properties of the system. For this reason, deforming the Hamiltonian may usually mean modifying the physical state itself. However, this turned out not always to be the case for a series of operation called sine-square deformation (SSD). The deformed Hamiltonian $\mathcal{H}_{\text{SSD}}$ is generated from the original Hamiltonian $\mathcal{H} = \int d\boldsymbol{r}\,\mathcal{H}(\boldsymbol{r})$ using an envelope function $f_{\text{SSD}}(\boldsymbol{r})$ as

$$\mathcal{H}_{\text{SSD}} = \int d\boldsymbol{r}\, f_{\text{SSD}}(\boldsymbol{r})\mathcal{H}(\boldsymbol{r}), \tag{1}$$

where $\boldsymbol{r}$ is a coordinate of the system with its origin at the center and

$$f_{\text{SSD}}(\boldsymbol{r}) = \frac{1}{2}\left[1 + \cos\left(\frac{\pi r}{R}\right)\right], \tag{2}$$

with R half the system length. As shown in Fig. 1, the sine-square function f_{SSD} governs the whole system by a single wavelength of $2R$ and $f_{\text{SSD}}(\boldsymbol{r})\mathcal{H}(\boldsymbol{r})$ varies smoothly from the maximum value at the center toward the edges. The SSD was proposed as one of the smooth boundary conditions to remove boundary effects [1,2], e.g., Friedel oscillations from the open boundaries, or artificial potentials that emerge for chosen cluster sizes and shapes which may stabilize fictitious orders [3]. The SSD Hamiltonian is empirically known to generate the wave function that recovers the translational symmetry, in perfect coincidence with the wave function under the periodic boundary condition [2,4]. This coincidence is proved in an *XY* model and a transverse-field Ising chain [5,6]. The SSD

ground state is also shown to serve as a restricted class of conformal field theories with some applications to a wider class of conformal mappings [7–12], and in that context the quantum dynamics of the SSD system is tested [13–17]. When an external field is applied, the physical quantities as a response function to the field are evaluated from the SSD Hamiltonian, whose accuracy against the exact solution in the thermodynamic limit is $O(10^{-4})$ [18].

From these studies, it is found that the SSD Hamiltonian loses its translational symmetry but could still or better reproduce the physical properties of the original Hamiltonian. A key to understanding this phenomenon is the idea of real-space renormalization [19], which stems from Wilson's poor man's scaling [20]. In a system with translational symmetry, a quantum state is characterized by a wave number. When the SSD is imposed, a wave number is no longer a quantum number, and a scattering term generated by $f_{\text{SSD}}(\boldsymbol{r})$ mixes these original eigenstates [21]. Such mixing generates a series of localized wave packets that serve as another basis set of the Hamiltonian. Since these states are localized, they are no longer influenced by the system size or by the boundary. Therefore, it allows us to obtain physical quantities that reproduce those in the thermodynamic limit [22].

In the present paper we apply this SSD to classical Ising models, as they provide a good platform to test approximate methods based on their exactly solvable structures [23]. The Hamiltonian of the *uniform* classical Ising model is

$$\mathcal{H} = \sum_{\langle \boldsymbol{\gamma}, \boldsymbol{\gamma}'\rangle} -J\sigma_{\boldsymbol{\gamma}}\sigma_{\boldsymbol{\gamma}'}, \tag{3}$$
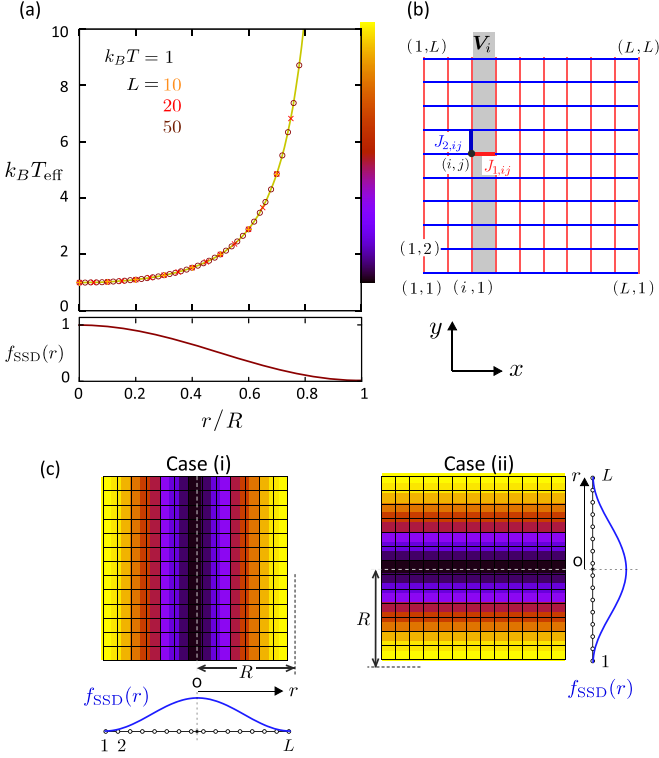
FIG. 1. (a) Change in effective temperature $k_B T_{\text{eff}}$ from the center ($r = 0$) toward the edge ($r/R = 1$) and the corresponding $f_{\text{SSD}}(r)$. (b) Two-dimensional square lattice with interactions $J_{1,ij}$ and $J_{2,ij}$ on bonds running in the positive directions of the x and y axes from site $\gamma = (i, j)$. The transfer matrix V_i is constructed in a unit of L sites in the y direction. (c) SSD along rows [case (i)] and columns [case (ii)].

with the uniform coupling constant J. The index γ represents a lattice site and the summation is taken over all the neighboring pairs of spins. The exact solutions are known for the one-dimensional (1D) chain and 2D square lattice. A second-order phase transition occurs in the 2D square lattice model at the temperature $k_B T_c = 2/\ln(1 + \sqrt{2}) \sim 2.2692 J$.

In constructing the SSD Ising Hamiltonian, we replace the uniform interaction J with $f_{\text{SSD}}(r)J$, where the position vector r is defined at the center of each bond. Suppose that the temperature of this deformed system is $k_B T$. Then the system can be regarded as an assemblage of Ising spins with uniform interactions at a renormalized effective temperature $k_B T_{\text{eff}} \equiv k_B T / f_{\text{SSD}}(r)$. Figure 1(a) shows an effective temperature as a function of r; the minimum value $k_B T_{\text{eff}}(r = 0) = k_B T$ at the center gradually increases toward infinity at the system edge.

The deformation in the 1D chain is straightforward. For the site index $i = 1, \ldots, L$ in Fig. 1(c), the bond connecting the ith and $(i + 1)$th sites is located at $r_i = i - L/2$, and we set $R = L/2$ to generate the value $f_{\text{SSD}}(r_i)$ in Eq. (2).

For the 2D square lattice, we consider an $L \times L$ lattice shown in Fig. 1(b) to keep the aspect ratio as unity [24] and define a coupling along the row between sites (i, j) and $(i + 1, j)$ as $J_{1,ij}$; its location is defined by $r_{1,ij}$. We take a bond along the column between sites (i, j) and $(i, j + 1)$ as $J_{2,ij}$ located at $r_{2,ij}$. Here the vectors $r_{1,ij}$ and $r_{2,ij}$ are not the ordinary position vectors but are introduced to define the

deformation function along the axis r parallel to the rows and columns for cases (i) and (ii), respectively, as shown in Fig. 1(c). We consider two cases. Case (i) deforms the bond interaction only along the row direction, keeping those along the column uniform; we plug into Eq. (2) $r_{1,ij} = i - L/2$ and $r_{2,ij} = i - (L - 1)/2$ with $R = L/2$. Case (ii) deforms the interaction along the column, while keeping the row direction uniform; we take $r_{1,ij} = j - (L - 1)/2$ and $r_{2,ij} = j - L/2$ for this case. The two cases formally differ in the analytical treatment as we show in Sec. III, where we construct the column-to-column transfer matrix.

The aim of this paper is to clarify the role of SSD in a classical Ising model. We show that the energy and related quantities accurately reproduce those of $k_B T_{\text{eff}}$, which means that one can obtain a set of data for a wide temperature range in a single calculation. The physical implication is that the SSD system is an assemblage of local subsystems with different temperatures, which form a modified canonical ensemble. The neighboring local subsystems have similar effective temperatures and work with each other as a heat bath. In Sec. IV we address the possibility of using other types of deformation.

The paper is organized as follows. In Sec. II we demonstrate that the transfer-matrix method is exactly applied to the SSD Ising model in one dimension. In Sec. III we analyze the 2D Ising model using a fermionic representation and obtain an exact form of the partition function for a finite system size for both case (i) and case (ii). Then we numerically evaluate the bond energy using these formulations in Sec. IV. We also perform a classical Monte Carlo simulation for the SSD Hamiltonian in Sec. IV C to test the numerical applicability of SSD. Section V gives a summary and discussion.

II. EXACT SOLUTION OF THE ONE-DIMENSIONAL SSD ISING MODEL

Let us first consider a partition function of a 1D periodic lattice consisting of L sites,

$$
\begin{aligned}
Z &= \sum_{\{\sigma_i\}} \exp\left(\sum_{i=1}^{L} K_i \sigma_i \sigma_{i+1}\right) \\
&= \sum_{\{\sigma_i\}} \prod_{i=1}^{L} \exp(K_i \sigma_i \sigma_{i+1}) = \text{Tr}\left(\prod_{i=1}^{L} V_i\right), \\
V_i &= \begin{pmatrix} e^{K_i} & e^{-K_i} \\ e^{-K_i} & e^{K_i} \end{pmatrix},
\end{aligned} \tag{4}
$$

using the conventional notation $K_i \equiv J_i/k_B T$ with $J_i \equiv J f_{\text{SSD}}(r_i)$. Here $r_i = i - L/2$ is the location of a bond connecting sites i and $i + 1$. The eigenvalues of the transfer matrix V_i are $\lambda_i^{\pm} = e^{K_i} \pm e^{-K_i}$, which explicitly depend on index i, whereas the corresponding eigenvectors $p_i^{\pm} = (1, \pm 1)/\sqrt{2}$ are site independent. In this way, all the transfer matrices are simultaneously diagonalized and the partition function is exactly given as

$$
Z = \prod_{i=1}^{L} \lambda_i^{+} + \prod_{i=1}^{L} \lambda_i^{-}. \tag{5}
$$

Then the exact expectation value of the bond energy is obtained as

$$\langle \sigma_i \sigma_{i+1} \rangle = \frac{(\lambda_i^-/\lambda_i^+)\prod_{l=1}^L \lambda_l^+ + (\lambda_i^+/\lambda_i^-)\prod_{l=1}^L \lambda_l^-}{\prod_{l=1}^L \lambda_l^+ + \prod_{l=1}^L \lambda_l^-}. \quad (6)$$

Taking the limit of an open boundary $J_L \to 0$, we find $\lambda_L^+ \to 2$ and $\lambda_L^- \to 0$, and the bond energy $\langle \sigma_i \sigma_{i+1} \rangle$ converges to

$$\frac{\lambda_i^-}{\lambda_i^+} = \tanh\left(\frac{J_i}{k_B T}\right) = \tanh\left(\frac{J}{k_B T_{\text{eff}}(\boldsymbol{r}_i)}\right). \quad (7)$$

Recalling that the energy per bond in the uniform system takes the form $e_{\text{bulk}} = -\tanh(J/k_B T)$ in the thermodynamic limit, one finds that the site-dependent bond energy of the SSD Hamiltonian is e_{bulk} at the local effective temperature $k_B T_{\text{eff}}(\boldsymbol{r}_i)$. The partition function at $L \to \infty$ is given as $Z = \prod_i \lambda_i^+$, which matches *exactly* the partition function of a system consisting of Ising bond degrees of freedom λ_i^+ with interaction J and i-dependent effective temperature $k_B T_{\text{eff}}(\boldsymbol{r}_i)$.

For later convenience, we show that Eq. (4) is written using the Pauli matrix τ^ν, $\nu = x, y, z$ (we use τ instead of σ to avoid confusion); unit matrix I; and the parameter K_i^*, which fulfills $\tanh K_i^* = e^{-2K_i}$ as

$$\begin{aligned} V_i &= e^{K_i}(I + \tau^x e^{-2K_i}) = (\tanh K_i^*)^{-1/2}(I + \tau^x \tanh K_i^*) \\ &= (\sinh K_i^* \cosh K_i^*)^{-1/2}(I \cosh K_i^* + \tau^x \sinh K_i^*) \\ &= (2 \sinh 2K_i)^{1/2} e^{K_i^* \tau^x}, \end{aligned} \quad (8)$$

where we use the relation $\sinh 2K_i \sinh 2K_i^* = 1$.

III. EXACT SOLUTION OF THE TWO-DIMENSIONAL SSD ISING MODEL

In this section we expand an analytical formula to compute the partition function Z of the SSD Ising model for a finite system size in two dimensions. The results shown here are also applied to deformations with functional forms other than f_{SSD}. Among several different approaches [23,25–32], we build our work based on the analysis given by Schultz *et al.* [32]. It provides a good description of the exact transfer matrix of the 2D Ising model by the 1D free fermionic degrees of freedom. In Sec. III A we give a review of this work originally applied to the uniform Hamiltonian and show that it can be applied to our system where the interactions are site dependent. We introduce the operators for the column-to-column transfer matrix in the fermionic representation and the related trace formula. Section III B is devoted to derivations of Z for cases (i) and (ii) with the SSD Hamiltonian, which uses the formula obtained in Sec. III A.

A. Preliminaries

1. Column-to-column transfer matrix

The explicit form of a transfer matrix V_i from column i to column $i + 1$ is given for a spatially nonuniform Hamiltonian as follows. Let $\boldsymbol{\sigma}_i \equiv \{\sigma_{i,j} \mid j = 1, 2, \ldots, L\}$ be a complete orthonormal basis of dimension 2^L of the ith column, where $\sigma_{i,j} = \pm 1$ is the Ising degrees of freedom on site (i, j) in Fig. 1(b). The operators $\hat{V}_{1,i}$ and $\hat{V}_{2,i}$ include the interactions along the ith column ($J_{1,ij}$) and jth row ($J_{2,ij}$), respectively,

and give a partition function Z as

$$Z = \text{Tr}\left(\prod_{i=1}^L \boldsymbol{V}_{1,i} \boldsymbol{V}_{2,i}\right),$$

$$\boldsymbol{V}_{1,i} \equiv \langle \boldsymbol{\sigma}_i, \boldsymbol{\sigma}_{i+1} | \hat{V}_{1,i} | \boldsymbol{\sigma}_i', \boldsymbol{\sigma}_{i+1}' \rangle$$

$$= \delta_{\boldsymbol{\sigma}_i, \boldsymbol{\sigma}_i'} \delta_{\boldsymbol{\sigma}_{i+1}, \boldsymbol{\sigma}_{i+1}'} \exp\left(\beta \sum_{j'=1}^L J_{1,ij'} \sigma_{i,j'} \sigma_{i+1,j'}\right),$$

$$\boldsymbol{V}_{2,i} \equiv \langle \boldsymbol{\sigma}_i | \hat{V}_{2,i} | \boldsymbol{\sigma}_i' \rangle = \delta_{\boldsymbol{\sigma}_i, \boldsymbol{\sigma}_i'} \exp\left((k_B T)^{-1} \sum_{j'=1}^L J_{2,ij'} \sigma_{i,j'} \sigma_{i,j'+1}\right).$$

$$(9)$$

Generalization of Eq. (8) to L degrees of freedom along the ith column immediately gives a description of $\boldsymbol{V}_{1,i}$ and $\boldsymbol{V}_{2,i}$ as

$$\boldsymbol{V}_{1,i} = \prod_{j'=1}^L (2 \sinh 2K_{1,ij'})^{1/2} \exp\left(\sum_{j=1}^L K_{1,ij}^* \tau_j^x\right),$$

$$\boldsymbol{V}_{2,i} = \exp\left(\sum_{j=1}^L K_{2,ij} \tau_j^z \tau_{j+1}^z\right), \quad (10)$$

with $K_{1;i,j} = J_{1,ij}/k_B T$ and $K_{2;i,j} = J_{2,ij}/k_B T$, where $K_{1,ij}^*$ is defined as $\tanh K_{1,ij} = e^{-2K_{1,ij}^*}$. We use a $2^L \times 2^L$ matrix defined as a direct product $\tau_j^\nu = I \otimes I \otimes \cdots \otimes \tau^\nu \otimes I \otimes \cdots \otimes I$, with τ^ν operating on the jth Ising degrees of freedom on the column. This form is further transformed first by rotating the axis of the Pauli matrices as $\tau_j^x \to -\tau_j^z$ and $\tau_j^z \to \tau_j^x$ and then by using a set of Pauli operators $\{\hat{\tau}_j^\nu\}$ operating on the jth site,

$$\hat{V}_{1,i} = \left(\prod_{j'=1}^L (2 \sinh 2K_{1,ij'})^{1/2}\right) \exp(\hat{H}_{1,i}),$$

$$\hat{V}_{2,i} = \exp(\hat{H}_{2,i}),$$

$$\hat{H}_{1,i} = \sum_{j=1}^L -K_{1,ij}^* \hat{\tau}_j^z,$$

$$\hat{H}_{2,i} = \sum_{j=1}^L K_{2,ij} \hat{\tau}_j^x \hat{\tau}_{j+1}^x, \quad (11)$$

where the trace of the operators over the 2^N Hilbert space gives $Z = \text{Tr}(\prod_{i=1}^L \hat{V}_{1,i} \hat{V}_{2,i+1})$.

By making use of the Jordan-Wigner transformation

$$\hat{\tau}_j^+ = \frac{1}{2}(\hat{\tau}_j^x + i\hat{\tau}_j^y) = \exp\left(-i\pi \sum_{l=1}^{j-1} c_l^\dagger c_l\right) c_j^\dagger,$$

$$\hat{\tau}_j^- = \frac{1}{2}(\hat{\tau}_j^x - i\hat{\tau}_j^y) = \exp\left(i\pi \sum_{l=1}^{j-1} c_l^\dagger c_l\right) c_j, \quad (12)$$

we obtain a fermionic representation of the operators as

$$\hat{H}_{1,i} = -\sum_{j=1}^L 2K_{1,ij}^* \left(c_j^\dagger c_j - \frac{1}{2}\right), \quad (13)$$

$$\hat{H}_{2,i} = \sum_{j=1}^L K_{2,ij}(c_j^\dagger - c_j)(c_{j+1}^\dagger + c_{j+1}), \quad (14)$$

where $c_j^\dagger$ (c_j) is a creation (annihilation) operator of spinless fermion. In the standard approach, the partition function is given as $Z = \mathrm{Tr}(\prod_{i=1}^L \hat{V}_i)$, with

$$\hat{V}_i = \hat{V}_{2,i}^{1/2} \hat{V}_{1,i} \hat{V}_{2,i+1}^{1/2} \quad (15)$$

an operator representing the column i–to–column $i + 1$ transfer matrix. If $\hat{V}_i$ does not depend on i, one is able to diagonalize the $2^L \times 2^L$ representation of $\hat{V}_i$, and the product of the largest eigenvalues will give Z. However, in case (i), since the transfer matrices depend on column i, they cannot be diagonalized simultaneously, and this approach does not straightforwardly apply. In the next subsection, we review the derivation of the exact solution for the uniform Ising model. The formula (16)–(20) will be adopted to calculate the partition function of case (i) in a later section. The eigenvalue solution of the transfer matrix of the uniform system is also to be compared with those obtained for the SSD Hamiltonian.

2. Spatially uniform 2D Ising model

For the interaction parameters $K_{1;i,j}$ and $K_{2;i,j}$, let us omit the row index j while keeping the column index i to clarify that it does not depend on j. Since the Hamiltonian is uniform along the column, the transfer matrix on the ith column is block diagonalized by using the Fourier transform of fermionic operators along the j direction,

$$c_j = \frac{1}{\sqrt{L}} e^{-i\pi/4} \sum_q e^{iqj} \eta_q, \quad (16)$$

where we take $q = (2l - 1)\pi/L$ and $2\pi l/L$ when the number of fermions $\mathcal{N} = \sum_q \eta_q^\dagger \eta_q$ is even and odd, respectively. The even- and odd-$\mathcal{N}$ sectors originate from the constraint imposed on Eq. (12) due to antiperiodic and periodic boundary conditions, respectively. The operators in Eqs. (13) and (14) are rewritten as

$$\hat{H}_{1,i} = \sum_{0 \leqslant q < 2\pi} \hat{H}_{1,iq},$$

$$\hat{H}_{2,i} = \sum_{0 < q < \pi} \hat{H}_{2,iq} + (\eta_0^\dagger \eta_0 + \eta_\pi^\dagger \eta_\pi),$$

$$\hat{H}_{1,iq} = -2K_{1,i}^* \left(\eta_q^\dagger \eta_q - \frac{1}{2} \right), \quad (17)$$

$$\hat{H}_{2,iq} = 2K_{2,i} \big(\cos q(\eta_q^\dagger \eta_q + \eta_{-q}^\dagger \eta_{-q}) + \sin q(\eta_q \eta_{-q} + \eta_{-q}^\dagger \eta_q^\dagger) \big), \quad (18)$$

where the last two terms of $\hat{H}_{2,i}$ with wave vectors $q = 0, \pi$ are present only in the odd-$\mathcal{N}$ sector. As the η_q with different $|q|$ commute, one can decompose the exponentials of the transfer matrix as

$$\hat{V}_i = (2 \sinh 2K_{1,i})^{L/2} \prod_q e^{\hat{H}_{2,iq}/2} e^{\hat{H}_{1,iq}} e^{\hat{H}_{2,i+1q}/2}. \quad (19)$$

We now prepare a matrix representation of Fock operators $e^{\hat{H}_{2,iq}/2}$ and $e^{\hat{H}_{1,iq}}$ by one-body states $|\eta_q\rangle = \eta_q^\dagger |0\rangle$, where

$\eta_q^\dagger = (\eta_q^\dagger, \eta_{-q})$:

$$H_{1,iq} = \langle \eta_q | \hat{H}_{1,iq} | \eta_q \rangle = \begin{pmatrix} -2K_{1,i}^* & 0 \\ 0 & 2K_{1,i}^* \end{pmatrix},$$

$$H_{2,iq} = \langle \eta_q | \hat{H}_{2,iq} | \eta_q \rangle = 2K_{2,i} \begin{pmatrix} \cos q & -\sin q \\ -\sin q & -\cos q \end{pmatrix} + 2K_2 \cos q. \quad (20)$$

The formulation in the rest of this section holds only when $H_{2,iq}$ does not depend on column index i; it is omitted from the interaction parameters as K_1 and K_2. We multiply $e^{H_{2,iq}/2 - K_2 \cos q} = I \cosh K_2 + (\cos q \tau^z - \sin q \tau^x) \sinh K_2$ and $e^{H_{1,iq}} = I \cosh 2K_1^* - \tau^z \sinh 2K_1^*$ using the Pauli matrices τ^ν and find a real symmetric matrix

$$e^{H_{2,iq}/2} e^{H_{1,iq}} e^{H_{2,i+1q}/2} = e^{2K_2 \cos q} \begin{pmatrix} A_q & C_q \\ C_q & B_q \end{pmatrix}$$

$$= e^{2K_2 \cos q} P \begin{pmatrix} e^{-2\epsilon_q^{(u)}} & 0 \\ 0 & e^{2\epsilon_q^{(u)}} \end{pmatrix} P^{-1}, \quad (21)$$

where in the final term we diagonalized the matrix by an orthogonal matrix P and $\epsilon_q^{(u)} \geqslant 0$ is obtained by the relationship

$$\cosh 2\epsilon_q^{(u)} = \cosh 2K_2 \cosh 2K_1^* - \sinh 2K_2 \sinh 2K_1^* \cos q. \quad (22)$$

By the same matrix P as in Eq. (21), the operator $\boldsymbol{\eta}_q$ undergoes a Bogoliubov transformation

$$\boldsymbol{\xi}_q = \begin{pmatrix} \xi_q \\ \xi_{-q}^\dagger \end{pmatrix} = P\boldsymbol{\eta}_q, \quad P = \begin{pmatrix} \cos \phi_q & \sin \phi_q \\ -\sin \phi_q & \cos \phi_q \end{pmatrix}. \quad (23)$$

Using this transformation, the product part of Eq. (19) is rewritten as $e^{\hat{H}_i}$, where the Fock operator $\hat{H}_i$ representing the transfer matrix is given as

$$\hat{V} = (2 \sinh 2K_1)^{N/2} \prod_{i=1}^L e^{\hat{H}_i},$$

$$\hat{H}_i = \sum_{0 < q < \pi} \left(-2\epsilon_q^{(u)} \xi_q^\dagger \xi_q + 2\epsilon_q^{(u)} \xi_{-q} \xi_{-q}^\dagger \right)$$

$$-2(K_1^* - K_2)\left(\eta_0^\dagger \eta_0 - \frac{1}{2} \right) - 2(K_1^* + K_2)\left(\eta_\pi^\dagger \eta_\pi - \frac{1}{2} \right)$$

$$= -\sum_{0 \leqslant q < 2\pi} 2\epsilon_q^{(u)} \left(\xi_q^\dagger \xi_q - \frac{1}{2} \right). \quad (24)$$

Here one can summarize all the q terms by reading off $\eta_0 = \xi_0$ and $\eta_\pi = \xi_\pi$, since we see from Eq. (22) that $\epsilon_0 = K_1^* - K_2$ and $\epsilon_\pi = K_1^* + K_2$.

The partition function is obtained [for reference, see Eq. (32) in the next subsection] as

$$Z = (2 \sinh 2K_1)^{N/2} \mathrm{Tr} \left(\prod_{i=1}^L e^{\hat{H}_i} \right)$$

$$= (2 \sinh 2K_1)^{N/2} \exp \left(L \sum_q \epsilon_q^{(u)} \right) \prod_q \left(1 + e^{-2L\epsilon_q^{(u)}} \right)$$

$$= (2 \sinh 2K_1)^{N/2} \prod_{0 \leqslant q < 2\pi} 2 \cosh \left(L\epsilon_q^{(u)} \right). \quad (25)$$
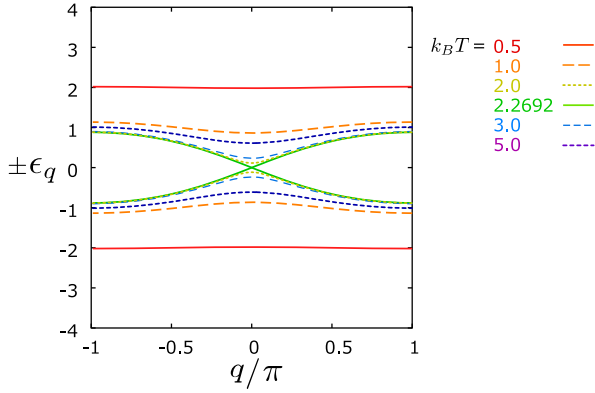
FIG. 2. Dispersion of fermions of a uniform Hamiltonian ϵ_q in Eq. (22) at several different temperatures.

The bond energy is written as

$$\langle \sigma_{i,j} \sigma_{i,j+1} \rangle = \sum_q - \frac{\tanh\left(L_1 \epsilon_q^{(u)}\right)}{\sinh 2\epsilon_q^{(u)}} (\sinh 2K_{2i} \cosh 2K_{1i}^*$$

$$- \cosh 2K_{2i} \sinh 2K_{1i}^* \cos q), \qquad (26)$$

$$\langle \sigma_{i,j} \sigma_{i+1,j} \rangle = - \frac{1}{\tanh 2K_{1i}} + \sum_q \frac{\tanh\left(L_1 \epsilon_q^{(u)}\right)}{\sinh 2\epsilon_q^{(u)} \sinh 2K_{1i}}$$

$$\times (\cosh 2K_{2i} \sinh 2K_{1i}^*$$

$$- \sinh 2K_{2i} \cosh 2K_{1i}^* \cos q). \qquad (27)$$

Considering only the contributions from the largest term in the product of the second equation in Eq. (25), which is valid for $L \to \infty$, we find

$$Z \to \Lambda_0 \equiv (2 \sinh 2K_1)^{N/2} \exp\left(L \sum_{0 \leqslant q < 2\pi} \epsilon_q\right), \qquad (28)$$

which reproduces the result in Ref. [32]. This corresponds to the vacuum state of the Bogoliubov quasiparticle, i.e., having $\langle \xi_q^\dagger \xi_q \rangle = 0$ for all q. In this limit, Eqs. (26) and (27) are modified to those for $\tanh(L_1 \epsilon_q) \to 1$.

Figure 2 shows pairs of $\pm \epsilon_q^{(u)}$ at several different temperatures. Here, by introducing a hole creation operator as an annihilation of particle $\bar{\xi}_q^\dagger = \xi_q$, Eq. (24) can be rewritten as

$$\hat{H}^i = - \sum_{0 \leqslant q < 2\pi} \epsilon_q^{(u)} (\xi_q^\dagger \xi_q - \bar{\xi}_q^\dagger \bar{\xi}_q), \qquad (29)$$

where the lowest-energy eigenstate of $\hat{H}^i$ is obtained by fully occupying a hole band and by keeping particle bands empty. This is a vacuum state of the Bogoliubov quasiparticle. Exciting a Bogoliubov quasiparticle $\langle \xi_q^\dagger \xi_q \rangle \neq 0$ corresponds to creating a particle-hole pair with the excitation energy $2\epsilon_q^{(u)}$ at wave number q. The gap at $q = 0$ closes at the transition temperature of the uniform 2D Ising model, $T_c = 2.2692$.

3. Full counting statistics and the trace formula

To count the full statistics Z consisting of column-dependent transfer matrices, we introduce another basic formula proved by Klich in Ref. [33]. Consider a second

quantized single-particle operator acting on the Fock space as

$$\hat{\Gamma}(\hat{A}) = \boldsymbol{c}^\dagger A \boldsymbol{c}, \quad \boldsymbol{c}^\dagger = (c_1^\dagger, \dots, c_M^\dagger), \qquad (30)$$

where A is the $M \times M$ matrix representation $A_{lm} = \langle l | \hat{A} | m \rangle$ of operator $\hat{A}$ on a single-particle Hilbert space of spinless fermions $\{|l\rangle\} = \{c_l^\dagger |0\rangle\}$, with a creation operator $c_l^\dagger$ ($l = 1, \dots, M$), applied on a vacuum $|0\rangle$. For two operators $\hat{A}$ and $\hat{B}$, we find $[\hat{\Gamma}(\hat{A}), \hat{\Gamma}(\hat{B})] = \hat{\Gamma}([\hat{A}, \hat{B}])$. We know from the Baker-Campbell-Hausdorff formula that for given matrices A and B, there is a matrix C that fulfills $e^A e^B = e^C$ [34]. Then the corresponding Fock operators are also given as

$$e^{\hat{\Gamma}(\hat{A})} e^{\hat{\Gamma}(\hat{B})} = e^{\hat{\Gamma}(\hat{C})}. \qquad (31)$$

As we will see shortly, this relationship guarantees that one can rewrite Eq. (15) in a single exponential form $e^{\hat{H}_i}$ as long as the operators $\hat{H}_{1,i}$, $\hat{H}_{2,i}$, and $\hat{H}_{2,i+1}$ are written by the common single-particle basis.

Any matrix C can be transformed to $P^{-1}CP = \text{diag}(\xi_1, \xi_2, \dots, \xi_M) + D$, with D an upper triangular matrix, where we are familiar with $D = 0$ for the symmetric matrix C. Since $\hat{\Gamma}(\hat{C}) = \sum_m \xi_m d_m^\dagger d_m + \sum_{i<j} D_{ij} d_i^\dagger d_j$, with $d_i = \sum_l P_{il}^{-1} c_l$, the trace of Eq. (31) is evaluated as

$$\text{Tr}(e^{\hat{\Gamma}(\hat{C})}) = \text{Tr}\left[\exp\left(\sum_m \xi_m d_m^\dagger d_m\right)\right]$$

$$= \det(I + e^{\text{diag}(\xi_m)}) = \prod_{m=1}^M (1 + e^{\xi_m})$$

$$= \det(I + e^A e^B). \qquad (32)$$

This trace formula holds for more than two products of exponentials of the operators. We apply this formula in obtaining Z for case (i).

B. Exact solutions of the deformed 2D Ising models

1. Case (i): When the Hamiltonian is uniform along the column and nonuniform along the row

In this subsection the parameters $K_{1;i,j}$ and $K_{2;i,j}$ depend on i but not on j, where we omit index j for simplicity. The formula (16)–(20) still holds. However, since the transfer matrix $\boldsymbol{V}_i$ depends on column index i and since $\boldsymbol{V}_i$ is no longer symmetric, we cannot straightforwardly prepare an orthogonal matrix P that diagonalizes all $\boldsymbol{V}_i$ simultaneously.

Instead of dividing Z into columns, we first take the whole product over the columns for each q to obtain $\hat{V}_q$ and then combine all q sectors as

$$Z = \prod_{i=1}^L (2 \sinh 2K_{1,i})^{L/2} \text{Tr}\left(\prod_q \hat{V}_q\right),$$

$$\hat{V}_q = \prod_{i=1}^L e^{\hat{H}_{2,iq}} e^{\hat{H}_{1,iq}} \equiv e^{\hat{H}_q}. \qquad (33)$$

We again find a final single exponential form of the Fock operator $\hat{H}_q$ since $\hat{H}_{1,iq}$ and $\hat{H}_{2,iq}$ fulfill the condition for $\hat{\Gamma}(\hat{A})$ and $\hat{\Gamma}(\hat{B})$ in Eq. (31). By multiplying the 2×2 matrix in Eq. (20),

we obtain an explicit form

$$e^{\hat{H}_q} = \boldsymbol{\eta}_q^\dagger \left(\prod_{i=1}^{L} e^{H_{2,iq}} e^{H_{1,iq}} \right) \boldsymbol{\eta}_q. \quad (34)$$

This matrix is diagonalized to $\mathrm{diag}(e^{-2E_q}, e^{2E_q})$ by performing a Bogoliubov transformation $(\eta_q^\dagger, \eta_{-q}) \to (\tilde{\xi}_q^\dagger, \tilde{\xi}_{-q})$ similarly to Eq. (23), and we find a final form

$$\hat{V}_q = \exp \left(\sum_{0 \leqslant q < 2\pi} -2E_q \left(\tilde{\xi}_q^\dagger \tilde{\xi}_q - \frac{1}{2} \right) \right). \quad (35)$$

Here $E_q \geqslant 0$ is an order-L quantity, which is the energy carried by the Bogoliubov quasiparticle $\tilde{\xi}_q$. In obtaining E_q, fermions η_q and η_{-q} mix for $0 < q < \pi$ so that the operator in Eq. (35) is represented by a 2×2 matrix, whereas for $q = 0$ and π, there is no mixing and we obtain $E_0 = \sum_i (K_{1,i}^* - K_{2,i})$ and $E_\pi = \sum_i (K_{1,i}^* + K_{2,i})$.

The partition function is obtained as

$$Z = \left(\prod_{i=1}^{L} (2 \sinh 2K_{1,i})^{L/2} \right) \prod_{0 \leqslant q < 2\pi} (e^{E_q} + e^{-E_q}). \quad (36)$$

Among the contributions from Bogoliubov quasiparticles to Z, namely, the last product term in the above equation, a so-called largest eigenvalue is obtained solely from a vacuum state of Bogoliubov quasiparticles as

$$\Lambda_0 = \left(\prod_{i=1}^{L} (2 \sinh 2K_{1,i})^{L/2} \right) \prod_{q} e^{E_q}, \quad (37)$$

and for $L \to \infty$ we obtain $Z = \Lambda_0$. Exciting a single Bogoliubov quasiparticle with a minimum excitation energy $2 \min(E_q)$ yields the next-largest eigenvalue so that $\Lambda_1/\Lambda_0 = e^{-2 \min(E_q)}$. The rest of the eigenvalues are determined by successively exciting quasiparticles $\prod_{q \in \{q\}_m} \xi_q^\dagger |0\rangle$, where $\{q\}_m$ is a set of indices of excited particles.

The energy densities per bond along the columns and rows are formally given as

$$\langle \sigma_{i,j} \sigma_{i,j+1} \rangle = -\frac{1}{L} \frac{\partial \ln Z}{\partial K_{2,i}} = -\frac{1}{L} \sum_{0 \leqslant q < 2\pi} \frac{dE_q}{dK_{2,i}},$$

$$\langle \sigma_{i,j} \sigma_{i+1,j} \rangle = -\frac{1}{L} \frac{\partial \ln Z}{\partial K_{1,i}}$$

$$= -\frac{1}{\tanh 2K_{1,i}} - \frac{1}{L} \sum_{0 \leqslant q < 2\pi} \frac{dE_q}{dK_{1,i}}. \quad (38)$$

In numerically evaluating these quantities, the derivatives are much less accurate than those we obtain for case (ii) in the next section.

2. Case (ii): When the Hamiltonian is nonuniform along the column and uniform along the row

In this subsection we consider case (ii). We start from Eqs. (13)–(15). From the discussion given in Sec. III A 3, the transfer-matrix operator in Eq. (15) is rewritten as $\hat{V}_i = e^{\hat{H}_{2,i}/2} e^{\hat{H}_{1,i}} e^{\hat{H}_{2,i}/2} = e^{\hat{H}_i}$, where $\hat{H}_i$ takes the quadratic form of a set of one-body operators $\{c_i\}$. Since the $\hat{V}_i$ do not depend on a column index i, their representations are separately diagonalized simultaneously for all columns. This time, however, the

Hamiltonian is nonuniform along the columns. Then the $L \times L$ matrix representation of $\hat{H}_i$ can no longer be block diagonalized into the smallest pieces by the Fourier transformation, nor can we apply the simple Pauli matrix representation we used in obtaining Eq. (21). Instead, the form of $\hat{H}_i$ is obtained through the following processes.

We first describe $\hat{H}_{1,i}$ and $\hat{H}_{2,i}/2$ in a quadric form of the one-body operators. Since the number of fermions is not conserved, we need to prepare a set of L-independent creation and annihilation operators. We reduce the $2L$ operators $\{c_j^\dagger, c_j\}$ $(j = 1, \dots, L)$ by half to avoid redundancy.[1] For this purpose, we use the reflection symmetry of f_{SSD} about the center of the system, $K_{2,ij} = K_{2,iL-j+1}$. The operators that fulfill $\mathcal{M}^{-1} a_j \mathcal{M} = -a_j$ and $\mathcal{M}^{-1} b_j \mathcal{M} = b_j$ about the parity operator $\mathcal{M}$ of the mirror reflection are

$$a_j^\dagger = \frac{1}{\sqrt{2}} (c_j^\dagger - c_{L-j+1}^\dagger),$$

$$b_j^\dagger = \frac{1}{\sqrt{2}} (c_j^\dagger + c_{L-j+1}^\dagger) \quad (39)$$

for $j = 1, \dots, \frac{L}{2}$. By using $\boldsymbol{\Phi}^\dagger = (b_1^\dagger, \dots, b_{L/2}^\dagger, a_1, \dots, a_{L/2})$, we obtain the expressions

$$\hat{H}_{1,i} = \sum_{j=1}^{L/2} -2K_{1,ij}^* (b_j^\dagger b_j - a_j a_j^\dagger), \quad (40)$$

$$\frac{\hat{H}_{2,i}}{2} = \boldsymbol{\Phi}^\dagger \begin{pmatrix} A^+ & B^- \\ -B^+ & -A^- \end{pmatrix} \boldsymbol{\Phi} - \mathrm{Tr}(A^+) + \mathrm{Tr}(A^-),$$

$$A_{mn}^\pm = \frac{K_{2,im}}{2} \delta_{m+1,n} + \frac{K_{2,in}}{2} \delta_{m-1,n} \pm \frac{K_{2,i(L/2)}}{2} \delta_{m(L/2)} \delta_{n(L/2)},$$

$$B_{mn}^\pm = \frac{K_{2,im}}{2} \delta_{m+1,n} - \frac{K_{2,in}}{2} \delta_{m-1,n} \pm \frac{K_{2,i(L/2)}}{2} \delta_{m(L/2)} \delta_{n(L/2)},$$

$$(41)$$

where $A^\pm$ and $B^\pm$ are the $\frac{L}{4} \times \frac{L}{4}$ matrices.

Next we find a matrix Q to transform $\boldsymbol{\eta}$ for $\hat{H}_{2,i}/2$ as

$$\boldsymbol{\eta}^\dagger = (\eta_1^\dagger, \dots, \eta_L^\dagger) = \boldsymbol{\Phi}^\dagger Q, \quad (42)$$

$$\frac{\hat{H}_{2,i}}{2} = \sum_{l=1}^{L} \gamma_l \eta_l^\dagger \eta_l. \quad (43)$$

Here γ_l, with $l = 1, \dots, \frac{L}{2}$, are non-negative and the other half with $\frac{L}{2} + 1, \dots, L$ are nonpositive. Since $e^{\hat{H}_{2,i}/2} = \sum_l e^{\gamma_l} \eta_l^\dagger \eta_l$, one can put this back into the original representation as

$$e^{\hat{H}_{2,i}/2} = \boldsymbol{\eta}^\dagger e^{\mathrm{diag}(\gamma_l)} \boldsymbol{\eta} = \boldsymbol{\Phi}^\dagger Q e^{\mathrm{diag}(\gamma_l)} Q^{-1} \boldsymbol{\Phi}. \quad (44)$$

We thus obtain the Fock operator

$$e^{\hat{H}_i} \equiv \boldsymbol{\Phi}^\dagger T \boldsymbol{\Phi},$$

$$T = Q e^{\mathrm{diag}(\gamma_l)} Q^{-1} e^{H_{1,i}} Q e^{\mathrm{diag}(\gamma_l)} Q^{-1}, \quad (45)$$

---

[1]One could also describe it using the Majorana fermions, while in that case the representation of the transfer matrix is given by an antisymmetric matrix which may be numerically rather bothersome to treat.

where from Eq. (40) we have $(e^{H_{1,i}})_{lm} = \delta_{lm} e^{-2K_{1,ij}^*}$ for $l \leqslant \frac{L}{2}$ and $\delta_{lm} e^{2K_{1,ij}^*}$ for $\frac{L}{2} + 1 \leqslant l$.

As a third step, we diagonalize Eq. (45) as $P^{-1}TP = \mathrm{diag}(\zeta_l)$, by a Bogoliubov transformation $\boldsymbol{\xi}^{\dagger} = (\xi_1^{\dagger}, \ldots, \xi_{L/2}^{\dagger}, \bar{\xi}_1, \ldots, \bar{\xi}_{L/2}) = \boldsymbol{\Phi}P$. Here the distribution of eigenvalues is such that half of the $\ln \zeta_l$ are nonpositive and the other half are non-negative. Therefore, by setting ζ_l in ascending order and by putting it back into the exponential form with $2\epsilon_l = |\ln \zeta_l|$, we find

$$\hat{V}_i = \left(\prod_{j=1}^{L} (2 \sinh 2K_{1,ij})^{1/2} \right) e^{\hat{H}_i},$$

$$\hat{H}_i = \sum_{l=1}^{L/2} -2\epsilon_l \xi_l^{\dagger} \xi_l + 2\epsilon_m \bar{\xi}_m \bar{\xi}_m^{\dagger}$$

$$= \sum_{l=1}^{L} -2\epsilon_l \left(\xi_l^{\dagger} \xi_l - \frac{1}{2} \right), \tag{46}$$

where for $m = l + \frac{L}{2}$ we have $\ln \zeta_m \geqslant 0$. We also apply a particle-hole transformation $\bar{\xi}_m \bar{\xi}_m^{\dagger} = 1 - \xi_m^{\dagger} \xi_m$. From Eq. (32) we find

$$\mathrm{Tr} \left(\prod_{i=1}^{L} e^{\hat{H}_i} \right) = \exp \left(L \sum_l \epsilon_l \right) \det[I + (e^{\mathrm{diag}(-2\epsilon_l)})^L]$$

$$= \prod_{l=1}^{L} (e^{\epsilon_l L} + e^{-\epsilon_l L}). \tag{47}$$

The partition function is obtained as

$$Z = \prod_{j=1}^{L} (2 \sinh 2K_{1,ij})^{L/2} \prod_{l=1}^{L} (e^{\epsilon_l L} + e^{-\epsilon_l L})$$

$$= \sum_{m=0}^{2^L - 1} \Lambda_m, \tag{48}$$

with $\Lambda_0 = \prod_{j=1}^{L} (2 \sinh 2K_{1,ij})^{L/2} \prod_{l=1}^{L} e^{\epsilon_l L}$ a partition function at $L \to \infty$. The bond energies along the columns and rows are given as

$$\langle \sigma_{i,j} \sigma_{i,j+1} \rangle = -\sum_{l=1}^{L} \tanh(L\epsilon_l) \frac{d\epsilon_l}{dK_{2,ij}}, \tag{49}$$

$$\langle \sigma_{i,j} \sigma_{i+1,j} \rangle = -\frac{1}{\tanh 2K_{1,ij}} - \sum_{l=1}^{L} \tanh(L\epsilon_l) \frac{d\epsilon_l}{dK_{1,ij}}. \tag{50}$$

Both $d\epsilon_l / dK_{1,ij}$ and $d\epsilon_l / dK_{2,ij}$ are evaluated using the elements of P and Q without taking the numerical derivative.

IV. NUMERICAL EXAMINATION

In this section we numerically demonstrate how SSD works on the Ising model by using the formula in the preceding section. We also compare these results with those of classical Monte Carlo simulations.

A. 1D systems

In Sec. II we found that the maximum eigenvalue of the transfer matrix on the bond at position $\boldsymbol{r}_i$ connecting sites i and $i + 1$ serves as a local partition function on that bond,

$$\lambda_i^+ = e^{-J/k_B T_{\mathrm{eff}}(r_i)} + e^{J/k_B T_{\mathrm{eff}}(r_i)}, \tag{51}$$

at its effective temperature $k_B T_{\mathrm{eff}}(r_i) = k_B T / f_{\mathrm{SSD}}(r_i)$. In the thermodynamic limit, the second largest eigenvalue λ_i^- is neglected and the total partition function becomes a product of λ_i^+. This means that the system is an ensemble of $L - 1$ different noninteracting bond degrees of freedom and unlike a uniform system, each is exposed to its own temperature $k_B T_{\mathrm{eff}}$ that depends on its location. The form of Eq. (51) indicates that one can obtain a set of equilibrium states with different temperatures $k_B T_{\mathrm{eff}}$ ranging from $k_B T$ to ∞, simultaneously, in a single system.

To examine how accurate the above-mentioned description would be at finite L, we numerically evaluate the bond energy of the SSD Hamiltonian in Eq. (6) as a function of $k_B T_{\mathrm{eff}}$ for several choices of $L = 4, \ldots, 100$, which is shown in Fig. 3(a). The bond energy even at $L = 4$ shows relatively good agreement with the exact bond energy $e_{\mathrm{bulk}} = -\tan(J/k_B T)$ of the $L = \infty$ uniform Ising model. The inset of Fig. 3(a) shows $\prod_i (\lambda_i^- / \lambda_i^+)$, which is a rapidly decreasing function of both $k_B T$ and L. When this quantity is sufficiently small, $Z = \prod_i \lambda_i^+$ holds, and λ_i^+ given in Eq. (51) serves as a local partition function for the corresponding local effective temperature, which is fulfilled for most of the temperature range $k_B T \gtrsim O(0.1J)$. Therefore, one can realize a canonical ensemble of systems with a variety of temperatures in a single system by properly setting $k_B T$.

Figure 3(b) shows the deviation of bond energy against e_{bulk}, which we call an SSD error. For $L \gtrsim 40$, it is less than 10^{-5}. Here a single partition function for a fixed $k_B T$ generates $L/2$-independent data points with different $k_B T_{\mathrm{eff}}$. Therefore, various $L/2$ sets of data are obtained by varying $k_B T = 0.1n$ with $n = 1, 2, \ldots$. The inset shows the SSD error of these series for $L = 10$; the data obtained near the system center are more accurate than those near the edges. We also found that the accuracy is improved for higher $k_B T$. We may explain this tendency by a slope of the effective temperature. The slope is gentle at the center and becomes steeper when approaching the edge of the system as shown in Fig. 1(a). The location that gives a certain fixed value of the effective temperature becomes closer to the system center if the system temperature $k_B T$ is higher. The local thermal equilibrium is better attained if an additional energy flow caused by the slope of the temperature can be neglected.

The results presented above are in good agreement with the tendency observed in the quantum many-body systems under the SSD. In the quantum cases [18], the physical quantities at $T = 0$ measured at the system center reproduce the values in the infinitely large system even when the system is as small as $L \lesssim 20$. At finite temperature, they work quite well even at $L = 4$ in the 1D system [35]. In the same context, the measurements of $-\langle \sigma_i \sigma_j \rangle$ in the present classical system are accurately performed near the system center by varying $k_B T$ even at small L. Generally, it is easy to increase L by one order of magnitude in classical systems, and the measurements
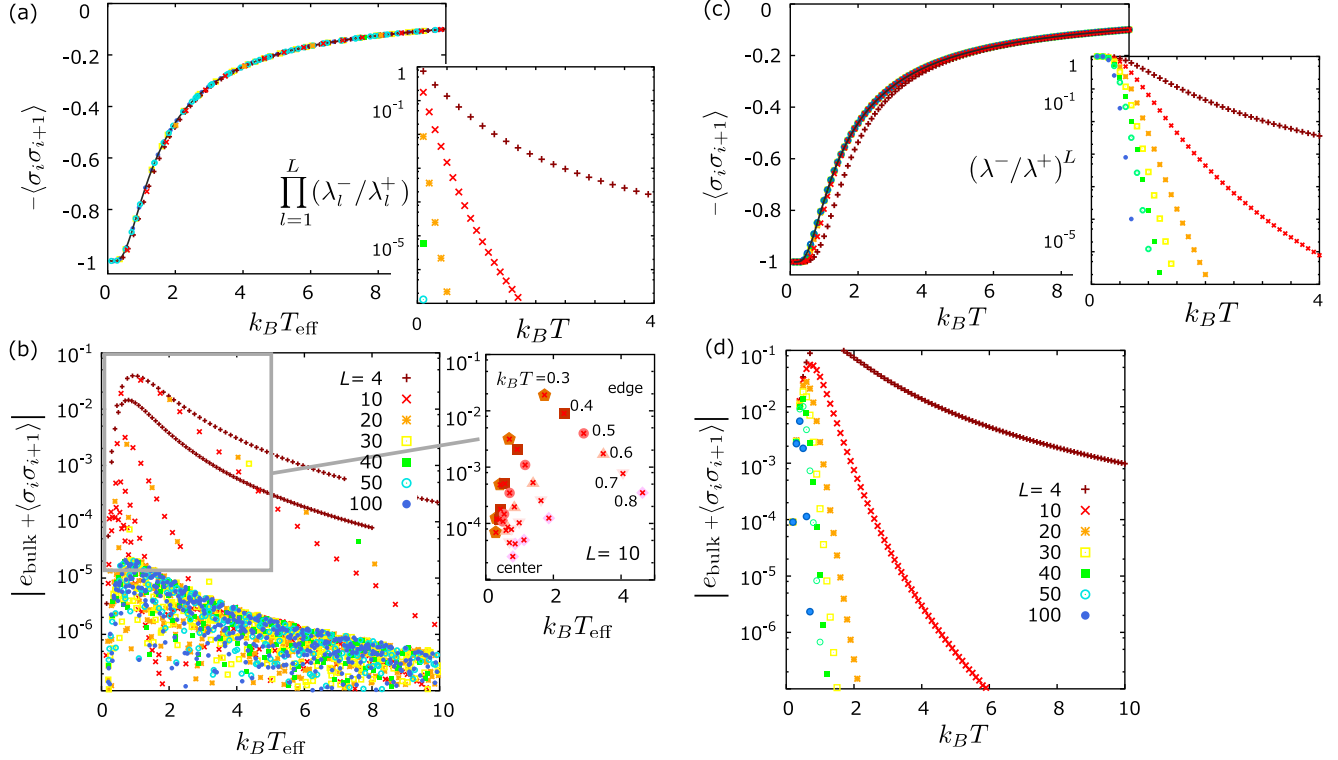
FIG. 3. Results of (a) and (b) the SSD Ising model in one dimension and (c) and (d) the uniform Ising model to be compared with (a) and (b). (a) Location (index-i)-dependent bond energy $-\langle\sigma_i\sigma_{i+1}\rangle$, given in Eq. (6), plotted against the effective temperature $k_B T_{\text{eff}}$ for $L = 4, \ldots, 100$. The solid line is the exact energy of a uniform Ising model e_{bulk} at $L = \infty$ as a function of temperature. (b) Deviations of bond energy in (a) from e_{bulk}. Calculations are done for several choices of $k_B T = 0.1n$ (n is an integer), where each single choice of $k_B T$ generates $L/2$ data points. The inset shows how the results vary with n for $L = 10$ magnified from the main panel; better accuracy is observed for the bonds closer to the system center. (c) Exact bond energy for $L = 4, \ldots, 100$ in the uniform 1D Ising model and (d) finite-size correction against e_{bulk}. The insets of (a) and (c) show $(\lambda^-/\lambda^+)^L$ as a function of temperature.

over a wide range of system become accurate enough [see Fig. 3(b)]. This fact will be of great advantage in utilizing the SSD for Monte Carlo simulations.

In Figs. 3(c) and 3(d) we show the results of a uniform Ising model at finite L to compare with Figs. 3(a) and 3(b), respectively. When λ^-/λ^+ (shown in the inset) becomes small enough, the bond energy approaches e_{bulk}. In contrast to the case of SSD, the bond energy at $L = 4$ disagrees with e_{bulk} by about 10^{-2}. An advantage of the SSD system over the uniform system is particularly significant at around $k_B T_{\text{eff}} \sim 1$. The finite-size correction of the uniform system remains of order 10^{-2} even when increasing L up to 100, where we find $\lambda^-/\lambda^+ \sim 1$ accordingly.

B. 2D systems

We apply the SSD along the rows in case (i) and along the columns in case (ii) [see Fig. 1(c)]. The fermionic dispersions along the columns, E_q/L in case (i) and ϵ_l in case (ii), are presented. For the SSD Hamiltonian, these two cases give different energy dispersions, since for case (i) q is a good quantum number along the columns but for case (ii) it is not. We checked that when J_{ij} is uniform, cases (i) and (ii), whose Hamiltonians are the same but the formulations differ, give the same results.

1. Fermionic dispersions

Let us first compare the energy dispersions of fermions as functions of q in the SSD and the uniform systems. The purpose here is to examine whether the partition function $Z \to \Lambda_0$ at $L \to \infty$ for the SSD in case (i) given in Eq. (37) is equivalent to the product of the local partition function of each column with different i-dependent $k_B T_{\text{eff}}(\mathbf{r}_i)$. The latter is formally obtained by replacing the uniform temperature $k_B T$ of Λ_0 with the i-dependent $k_B T_{\text{eff}}(\mathbf{r}_i)$ in Eq. (28) in Sec. III A 2. This replacement is equivalent to having the relation

$$\sum_{i=1}^{L} \epsilon_q^{(u)} = E_q, \tag{52}$$

where $\epsilon_q^{(u)}$ of the uniform system calculated for each $k_B T_{\text{eff}}(\mathbf{r}_i)$ is summed over different columns on the left-hand side and E_q on the right-hand side is obtained in Eq. (37). If this equation exactly holds, the classical SSD system in two dimensions is an extended canonical ensemble of local subsystems, each in an equilibrium of different temperature. Since E_q cannot be obtained analytically, we show numerically that this relationship holds almost exactly except for the small deviation at around $q \sim 0$.

Figure 4(a) shows E_q/L in Eq. (35) for case (i) with $L = 50$ for several choices of $k_B T$. Since E_q is the order-L
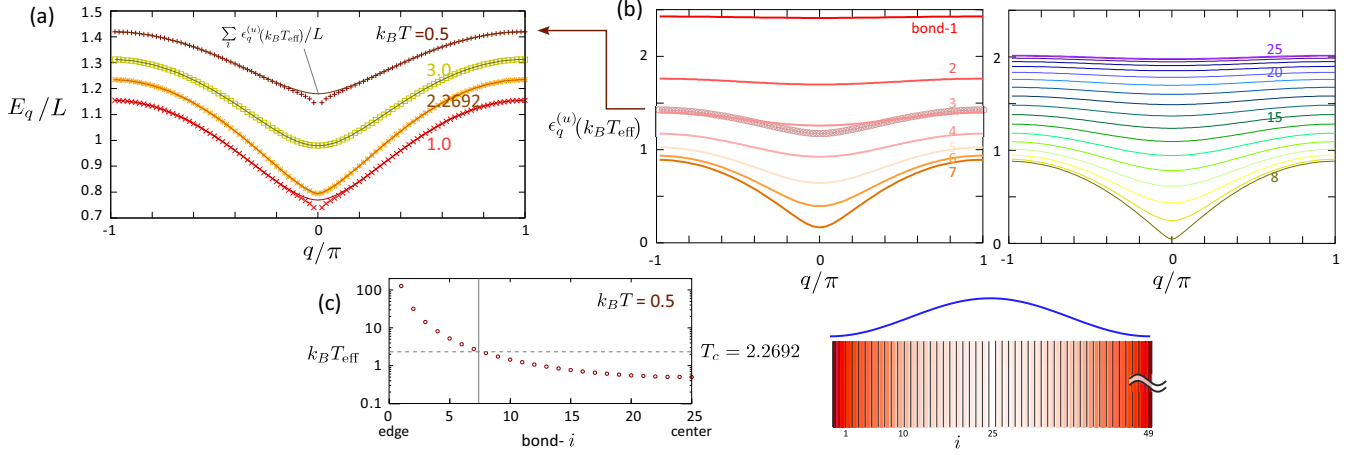
FIG. 4. Dispersions of fermions of a transfer matrix along the columns (j direction) with $L = 50$ in case (i): (a) E_q/L in Eq. (35) for case (i) with $L = 50$ (symbols) at $k_BT = 0.5$, 1, 2.2692($= k_BT_c$), and 3; (b) $\epsilon_q^{(u)}$ obtained using Eq. (22) with the temperature k_BT_{eff} that depends on the location of bond i, $i = 1, \ldots, 25$; and (c) i-dependent k_BT_{eff} used to evaluate the dispersions in (b). The solid lines in (a) are the summation of $\epsilon_q^{(u)}$ throughout the system, $i = 1, \ldots, 50$, to be compared with E_q for the same system temperature k_BT. The right panel in (c) is the density plot of k_BT_{eff}, together with the profile of f_{SSD} along the rows.

quantity obtained after multiplying the transfer matrices of all columns, we expect that it can be approximately divided into contributions from different columns if these columns can be regarded as independent subsystems, which is the implication of Eq. (52). In Fig. 4(b) we plot a set of $L/2$-independent dispersions of fermions representing a single transfer matrix of a uniform system $\epsilon_q^{(u)}$, each obtained for column (bond i)-dependent k_BT_{eff} using Eq. (22). A set of effective temperatures k_BT_{eff} for $k_BT = 0.5$ adopted in this calculation is shown in Fig. 4(c). At $i = 1, \ldots, 7$ where $k_BT_{eff} \leqslant k_BT_c$ in the left panel, the dispersion is a descending function of i, and then for $i \geqslant 8$ in the right panel it ascends with i. By averaging all the dispersions over $i = 1, \ldots, L$, the data points in Fig. 4(b) (brown symbols in the left-hand-side panel) are obtained, which are the same data as those plotted as a solid line in Fig. 4(a) marked by arrows. We find that, except for the vicinity $q/\pi \sim 0$, the average $\sum_i \epsilon_q^{(u)}/L$ and E_q/L are in almost perfect agreement. The same comparison holds for other k_BT.

In this way, the contributions to E_q from each column are well approximated by $\epsilon_q^{(u)}$ under locally defined effective

temperature k_BT_{eff}. The result indicates that a picture we proved in one dimension also holds in two dimensions, namely, the system can be regarded as an assemblage of small subsystems having a different canonical temperature k_BT_{eff}.

2. Bond energy

Since we found that the 2D SSD system can simultaneously host $L/2$ different subsystems with different effective temperature, we can use this fact to evaluate the local physical quantities in each subsystem. Figure 5(a) shows the bond energy $-\langle \sigma_\gamma \sigma_{\gamma'} \rangle$ as a function of k_BT_{eff} obtained for case (ii) using Eqs. (49) and (50), where we set $k_BT = 0.5$ and plot the results for $L = 10, \ldots, 500$. The solid line e_{bulk} is an exact solution of the $L = \infty$ uniform Ising model. The data at $L = 10$ still deviate from e_{bulk}, but when $L \gtrsim 50$ they almost perfectly overlap with e_{bulk}. The SSD error $|e_{bulk} + \langle \sigma_\gamma \sigma_{\gamma'} \rangle|$ for the same data set is shown in Fig. 5(b). There are two series of data points following different curves for the same value of L. One is the bond energy evaluated along the columns and the other one is along the rows. The error is suppressed to less
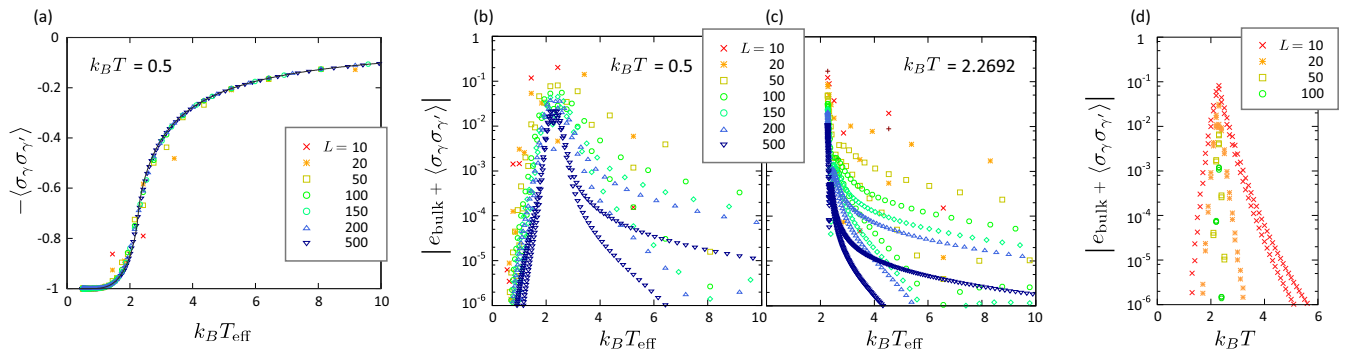

FIG. 5. (a) Bond energy $-\langle \sigma_\gamma \sigma_{\gamma'} \rangle$ evaluated for the 2D SSD Ising model plotted against k_BT_{eff} using Eqs. (49) and (50) for case (ii) with $L = 10, \ldots, 500$ and $k_BT = 0.5$. The solid line is the exact bulk energy ϵ_{bulk}. (b) SSD error $|e_{bulk} + \langle \sigma_\gamma \sigma_{\gamma'} \rangle|$ for the data in (a) with $k_BT = 0.5$. (c) SSD error for a set of bond energies evaluated for $k_BT = 2.2692 = k_BT_c$. (d) Finite-size corrections of the bond energy evaluated for the uniform 2D system using Eqs. (49) and (50) as a function of k_BT.
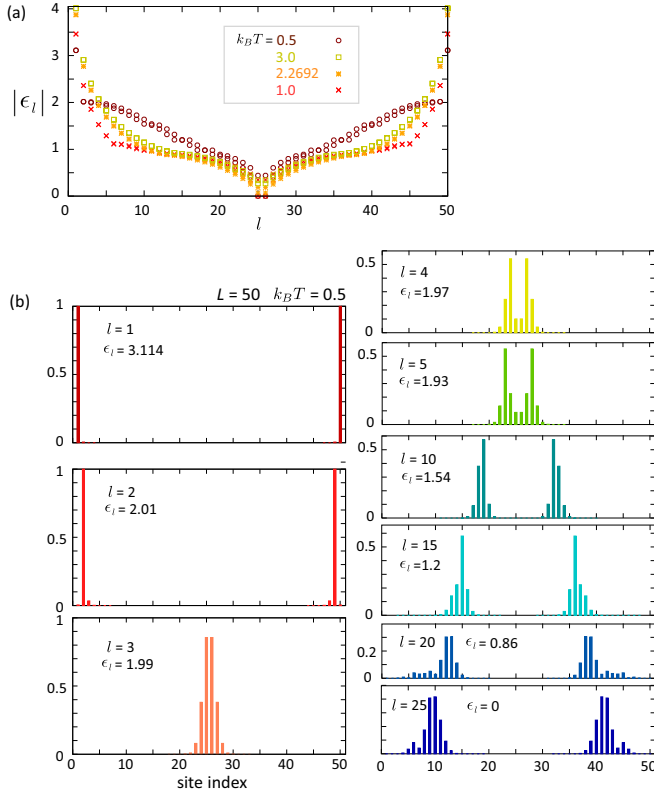
FIG. 6. (a) Dispersions ϵ_l of fermions of a transfer matrix along the columns (j direction) with $L = 50$ in Eq. (46) for case (ii) with $k_B T = 0.5$, 1, 2.2692($= k_B T_c$), and 3. (b) Spatial amplitude of the one-body eigenstate of index l calculated at $L = 50$ and $k_B T = 0.5$ in (a). The bottom panel for the $l = 25$ state is the zero-energy state.

than 10^{-3} in a wide range of $k_B T_{\text{eff}}$ when $L \gtrsim 100$. Setting $k_B T$ to $k_B T_c$ further suppresses the SSD error as shown in Fig. 5(c). This is because the spatial slope of the effective temperature becomes gentle at the critical temperature $k_B T_c$ where the finite-size effect is very strong. The local subsystem can more easily attain the thermodynamic equilibrium at the target effective temperature when the differences of $k_B T_{\text{eff}}$ with its neighbors are smaller. For comparison, we also calculate the bond energy of a uniform system and plot a finite-size error in Fig. 5(d). They are calculated using Eqs. (26) and (27). Near $T_c \sim 2.2692J$, the correlation length diverges and the finite-size effect becomes large. This fact is consistent with the peak of SSD error near $k_B T_{\text{eff}}$.

3. Eigenstates of fermions

We now examine the spatial distribution of wave functions of fermions when case (ii) SSD is applied. Figure 6(a) shows the energy levels ϵ_l of fermions obtained using Eq. (46). We plot the data for several choices of $k_B T$. Since the column direction is no longer uniform, the label l is not a wave number but an index in descending order of ϵ_l for $l = 1, \ldots, 25$. The latter half, $l = 26, \ldots, 50$, takes the same values as the former half due to the reflection symmetry.

Following Refs. [18,21], we first explain how the SSD term reorganizes the eigenstates of fermions. By introducing

$f_{\text{SSD}}(j) = 1 - g(j)$, which fulfills $g(j) = g(L + 1 - j)$,

$$g(j) = \cos\left[\frac{2\pi}{L}\left(j - \frac{1}{2}\right)\right] = g_1 e^{i\delta j} + g_{-1} e^{-i\delta j},$$

$$g_1 = g_{-1}^* = \frac{e^{i\delta/2}}{2}, \tag{53}$$

where $\delta = 2\pi/L$, one could separate the exponent of Eq. (14) into two parts as

$$\hat{H}_{2,i} = \sum_q \hat{H}_{2,iq} - \sum_\pm \hat{H}_{d\pm}, \tag{54}$$

$$\hat{H}_{d\pm} = g_{\pm1}\left[\sum_q 2\cos\left(q \mp \frac{\delta}{2}\right)\eta_q^\dagger \eta_{q\mp\delta} \right.$$

$$\left. + \sum_{0 \leqslant q \leqslant \pi} 2\sin\left(q \mp \frac{\delta}{2}\right)(\eta_q^\dagger \eta_{-q\pm\delta}^\dagger + \eta_{-q}\eta_{q\mp\delta})\right]. \tag{55}$$

The first term of Eq. (54) is a q component of Eq. (18). In the uniform system, the eigenstate is characterized by a wave number q. By introducing the SSD, one-body states of different values of q mix as in Eq. (55). The particular form of f_{SSD} allows this mixing only between neighboring q which are discretized in units of $\delta = 2\pi/L$. The amplitude of mixing also depends on q. It takes the largest values at $q = 0$ and π for the first term and at $q = \pm\pi/2$ for the second term. These three are the top or bottom and the middle of the energy band in Fig. 6(a), respectively. Such moderate mixing generates a wave packet as an eigenstate of $\hat{H}_{i,2}$. Strictly speaking, the final eigenstates are those of Eq. (45) and not of $\hat{H}_{2,i}$, but once we already have a wave-packet state localized in real space, it does not change much by the operation of $e^{H_{1,i}}$, as it has only a diagonal form in the real-space representation.

In Fig. 6(b) the weight of the one-body state ($\bar{\bar{\xi}}_l^\dagger|0\rangle$) at a site j, $|(Q_i)_{jl}|$, for the dispersion of the fermions at $k_B T = 0.5$ in Fig. 6(a) is shown for several energy levels l. Those labeled by $l = 1, 2$ are the ones providing the two largest ϵ_l and are almost completely localized at the edge sites. This is because the coefficients in Eq. (55) is the largest and it efficiently mixes the states over the wide range of wavenumbers so that the wave packets become a δ function. In all energy levels in Fig. 6(b), the wave packet typically spans at most three to four lattice spacings and carries a bulk energy ϵ_l, which gives a rough characteristic energy scale of $k_B T_{\text{eff}}$. In the uniform and finite systems, the size effect in the quantum state occurs because they are plane waves with discretized wave number. However, for SSD, the wave-packet state is localized and does not feel the size of the system. Their local physical quantities behave nearly scale-free [22]. This wave-packet-type distribution of fermions in real space supports the picture that the system is an assemblage of local subsystems at different effective temperatures.

C. Monte Carlo simulation

We solved the classical Ising model in a finite system size exactly using the fermionic representation. However, even in the classical systems, the cases with exact solutions are
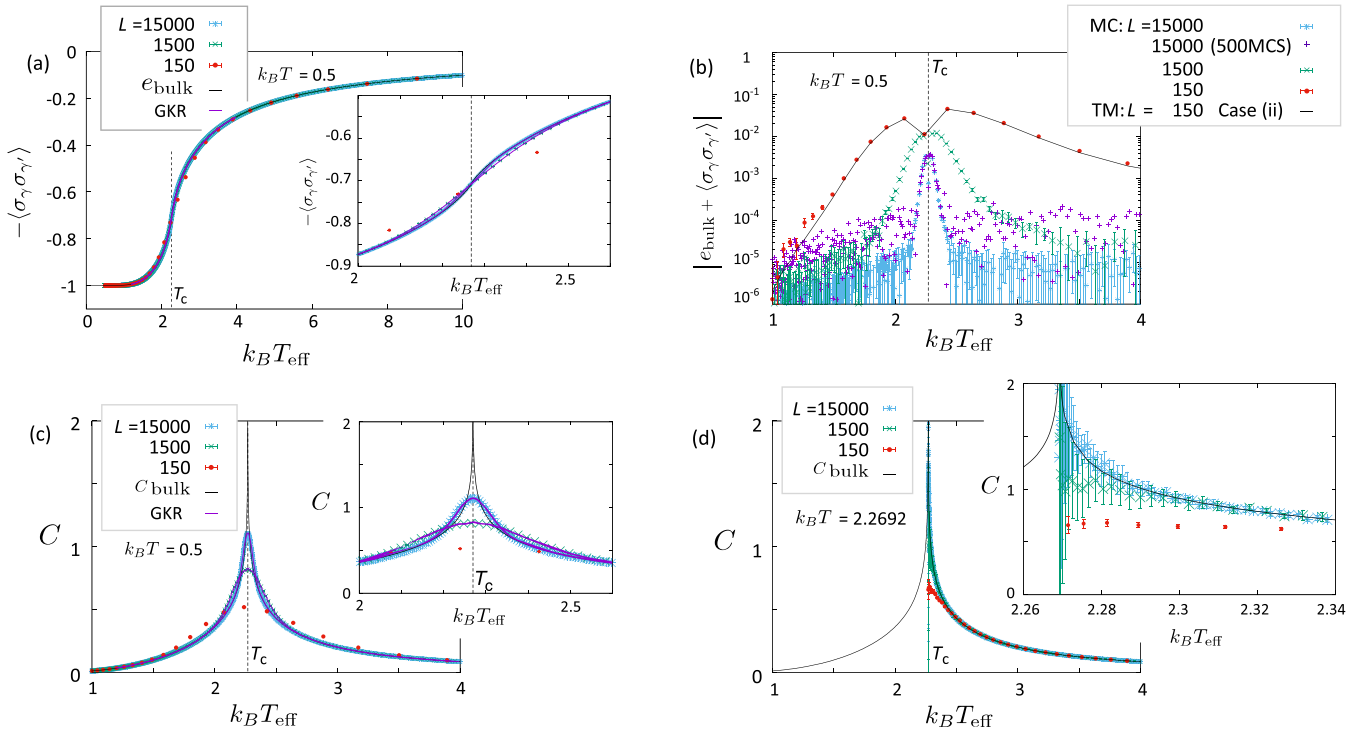
FIG. 7. Results obtained by the classical Monte Carlo simulations in the 2D Ising model with the SSD in one direction. The simulation temperature is denoted by $k_B T$, which corresponds to the lowest effective temperature. After discarding the initial 5000 steps, we measured the bond energy for 50 000 steps unless specified otherwise. The insets show enlarged views near the critical temperature. (a) Bond energy plotted against the effective temperature of each column. We compare our results of different lattice sizes with the exact bulk energy e_{bulk} and the result of Gaussian kernel regression (GKR). (b) The SSD error. The MC results of $L = 150$ are consistent with the transfer-matrix (TM) results shown by the solid line for case (ii) with SSD of the same size. We also plotted the result of $L = 15\,000$ measured for 500 MCSs to check the MCS dependences. (c) and (d) Results of the specific heat compared with the exact bulk value c_{bulk} and the GKR results.

limited. A Monte Carlo (MC) simulation usually serves as a good approximate solver. Applying the SSD to an MC simulation raises the question of whether an SSD system converges to a proper equilibrium state even though the effective temperature of each spin depends on the location. We thus carried out the standard single-spin-flip MC simulations to the 2D Ising model deformed in one direction. The effective temperature differs for each column as shown in Fig. 1(c). We collected the bond energy for each column separately and plotted it against the effective temperature. We discarded the first 5000 MC steps (MCSs) and measured the bond energy for 50 000 MCSs after that. We also performed ten independent MC runs and took an average of the data. The initial spin configuration is the ferromagnetic state with $\sigma_\gamma = 1$.

Figure 7 shows the MC data obtained for different system sizes. We checked that the MC result of $L = 150$ is consistent with that of the transfer-matrix method shown in Fig. 5. As shown in Fig. 7(a), the temperature dependence of the bond energy agrees well with the exact results for the whole temperature region. We find a small discrepancy only in the vicinity of the critical temperature, which decreases as the system size increases. The trend is clearly observed in the plot of the SSD error in Fig. 7(b). Both a peak value at $T_{eff} = T_c$ and the width are found to scale with $1/\sqrt{L}$. We also plot in this figure a result of $L = 15\,000$ measured only for 500 MCSs after discarding 5000 steps. The peak shape at T_c is the same as the original measurement with 50 000

MCSs, but the base of the peak is shifted upward roughly by one order of magnitude ($\sim$10 times), which is the ratio of a square root of two MCSs. Therefore, the SSD error in this off-critical region is controlled by the standard MC statistical error $(1/\sqrt{MCS}) \times (1/\sqrt{L})$. This suggests that the MC approximation would become exact in the limit of an infinite number of steps in this off-critical region of the SSD system. On the other hand, the SSD error in the critical region near $T = T_c$ is due to the systematic one that solely depends on L.

We confirm the validity of the present SSD simulation by examining how precisely we can reproduce the specific heat from our data. The specific heat is usually evaluated as a fluctuation of energy based on the two-point correlation of the bond energy over the whole system. However, the correlations between different bonds no longer makes sense when the SSD is applied. Instead, we evaluate it from the derivatives of $-\langle \sigma_\gamma \sigma_{\gamma'} \rangle$ against $k_B T_{eff}$. It is easily performed by the difference between the neighboring effective-temperature data. As shown in Fig. 7(c), the specific heat C is also consistent with the exact result for the off-critical temperature region. The SSD error of the specific heat is consistent with that of the bond energy shown in Fig. 7(b).

Recall that a massive number of temperature data are generated in the SSD simulation only by a small numerical effort. Taking full advantage of this, we apply the Gaussian kernel regression (GKR) coupled with the Bayesian inference [36]. The GKR is a machine-learning-based statistical data analysis

and with this we can estimate the critical temperature and can also obtain bond energy as a continuous function of temperature without assuming any analytical function form. Since a larger number of data sets gives a better performance of GKR, our SSD MC simulation provides a suitable playground for it. In our case, the specific heat is obtained continuously without taking the numerical derivatives. We only need to take an analytic derivative of the Gaussian distribution function used there. The regression was already proved to reproduce the critical temperature of the classical 2D Ising model within an accuracy of 10^{-6} and the state-of-art temperature-dependent critical exponent that converges to $\beta = \frac{1}{8}$ at $T = T_c$ [37].

We randomly choose 500 data in a range of $1.2 \leqslant T \leqslant 4.0$ and apply the GKR by setting the regression variables (x_i, y_i) as $x_i = -\langle \sigma_\gamma \sigma_{\gamma'} \rangle - E_c$ and $y_i = k_B T_{\text{eff}} - k_B T_c$, where T_c and E_c (the bond energy at the critical temperature) are parameters to be estimated by the Bayesian inference. Here we exchange x_i and y_i from the conventional definition because the bond energy exhibits a singular behavior at $T = T_c$. It is much easier for the regression to model a function with a gentle slope than to model a function with a steep slope. We also know that the specific heat is symmetric and the bond energy is antisymmetric by a mirror reflection of the temperature at the critical temperature in the critical region. To take this prior information into account, we introduce a set of mirror data [38] with respect to the critical point as $x'_i = -x_i$ and $y'_i = -y_i$. We mix the data below and above the critical temperature only in the critical temperature region $|y_i| < \Delta T$, where ΔT, which is the width of the critical region, is another parameter to be estimated by the Bayesian inference. The GKR results of $L = 1500$ and 15 000 are plotted with lines in Figs. 7(a) and 7(c). The estimated critical temperature and the bond energy values are $(T_c, E_c) = (2.2702(3), -0.7072(2))$ for $L = 1500$ and $(T_c, E_c) = (2.2699(2), -0.7065(2))$ for $L = 15\,000$, whereas the exact bulk values are $(T_c, E_c) = (2.2692\ldots, -0.707\,10\ldots)$. The width of the critical region is estimated as $\Delta T = 0.150(7)$ for $L = 1500$ and $\Delta T = 0.11(1)$ for $L = 15\,000$. The critical temperature and the bond energy deviate from the exact results only by an order of 10^{-4}. Our data in the vicinity of the critical temperature include the SSD error by an order of 10^{-3} to 10^{-2} as shown in Fig. 7(b). The difference between the neighboring effective temperatures at T_c is more than 10^{-3} even in the system of $L = 15\,000$. The Bayesian inference realizes an accuracy almost ten times better than these SSD errors.

Since the SSD approximation is generally good at the center of the system, we can reduce the SSD error in the critical region by setting the simulation temperature to the critical temperature [in the same context as shown in Figs. 5(b) and 5(c)]. Figure 7(d) shows the result of the specific heat. The error bars near T_c are much larger than the result of $k_B T = 0.5$. The present number of MCSs may not be sufficient because a real simulation temperature is a critical temperature and a critical slowing down may occur. In this model, the specific heat diverges at T_c. The exact solution shows that the specific heat reaches $C \sim 2$ when the temperature approaches $|T - T_c| = 4 \times 10^{-4}$. This exact value is reproduced by the Monte Carlo simulation data for $L = 15\,000$ within the error bar.
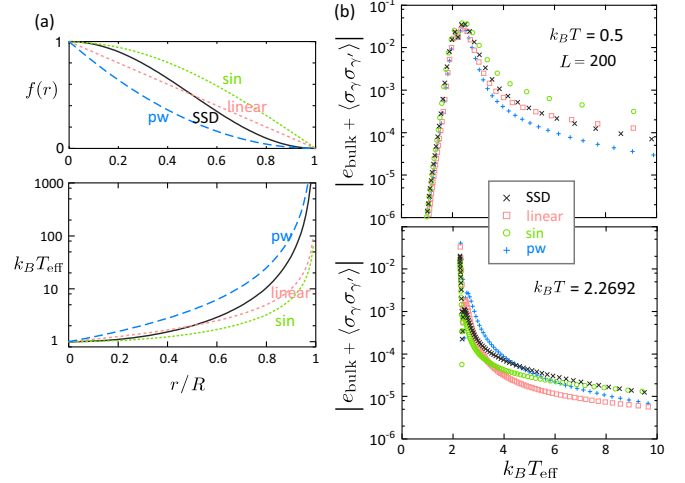

FIG. 8. (a) Functional form of Eq. (58) and SSD, and the corresponding effective temperature $k_B T_{\text{eff}}$ as functions of r/R. (b) Deformation error $|e_{\text{bulk}} + \langle \sigma_\gamma \sigma_{\gamma'} \rangle|$ calculated using case (ii) by replacing the SSD functions with the three other functions given in Eq. (58). The bond energies for different $k_B T_{\text{eff}}$ are obtained at different locations of the system of $L = 200$ along the rows.

D. Other deformation functions

So far we have studied the effect of SSD on classical Ising models. However, unlike for the quantum models, our results may suggest that the SSD is not the special deformation for classical models. To clarify this point, we perform the same calculation as case (ii) for other envelope functions. We adopt three functions

$$f_{\sin}(r) = \sin \left[\frac{\pi}{2} \left(1 - \frac{r}{R} \right) \right], \tag{56}$$

$$f_{\text{linear}}(r) = 1 - \frac{r}{R}, \tag{57}$$

$$f_{\text{pw}}(r) = \left(1 - \frac{r}{R} \right)^2 \tag{58}$$

whose spatial dependence and corresponding $k_B T_{\text{eff}}$ as functions of r/R are shown in Fig. 8(a). We find that the slopes of $f_{\sin}(r)$ and $f_{\text{pw}}(r)$ are decreasing and increasing functions of r/R, while the slope of $f_{\text{linear}}(r)$ is a constant; the slope of SSD is first a decreasing function and then becomes an increasing function. Figure 8(b) shows two panels with different system temperatures $k_B T = 0.5$ and $2.2692 (= k_B T_c)$ calculating the deformation error (SSD error) of the bond energy along the rows as a function of $k_B T_{\text{eff}}$. For $k_B T = 0.5$, f_{pw} gives a smaller deformation error than the other three, but for $k_B T = 2.2692$ the same f_{pw} gives the largest deformation error. The ones for $f_{\sin}$ and f_{linear} also have different tendencies depending on $k_B T$. This is because the deformation error overall tends to increase as the slope $d(k_B T_{\text{eff}})/dr$ becomes larger, as we discussed previously. The temperature slope at each $k_B T_{\text{eff}}$ varies depending on the system temperature and the choice of envelope functions. However, since the slope of SSD varies with a moderate tendency compared to the other three cases and we have the optimal zero slope $d(k_B T_{\text{eff}})/dr = 0$ at both $r/R = 0$ and 1, it is sustained as a moderately stable function,

not depending much on the system parameters. Therefore, although one may choose other functions for their purposes, the SSD may be regarded as an optimal function in the sense that it does not require tuning of parameters.

V. SUMMARY AND DISCUSSION

We analyzed the 1D and 2D ferromagnetic Ising models with spatially deformed interactions in the sine-square functional form. We found that this interaction-deformed system is equivalent to the uniform-interaction system with spatially deformed temperature. To be more precise, we showed by analytical and numerical analyses that this deformed classical system is an assemblage of small subsystems. Each subsystem locally realizes the equilibrium of a uniform system at its own effective temperature. We proposed that this classical SSD at finite temperature gives an approximate extended canonical ensemble with its state indices spanning real space.

In the analytical calculation, we first extended the formulation of the conventional transfer-matrix method to that of the nonuniform system. We showed that the partition function is exactly obtained even though the interaction is deformed in one direction; this fact is rather trivial in one dimension, as the eigenstate of the transfer matrix defined on each bond does not depend on the strength of the interactions. In two dimensions the transfer matrices are defined in a unit of a column of the lattice of length L, describing the contributions from 2^L different configurations of the Ising variables. Referring to the previously established approach, the Ising variables are transformed to the noninteracting 1D fermionic operators, and 2^L ensemble averages of the Ising variables are mapped to the summation of 2^L different many-body states constructed from the noninteracting one-body states of Bogoliubov fermions. For demonstration, these formulas were numerically evaluated in 1D and 2D Ising models with SSD for system size $L = 10$–500. Note that it is practically possible to extend it to $L \gtrsim 10\,000$ if needed, as it is a one-body problem of fermions on a chain of length L. In the uniform 2D system, the above-mentioned Bogoliubov quasiparticles are itinerant

plane waves characterized by wave numbers, but once the SSD turns on, they mix via scattering of the SSD potential and form a set of spatially localized wave-packet states. At the same time, according to our picture, a system with spatially nonuniform interaction bonds J_i at the temperature $k_B T$ could be interpreted as a spatially uniform system with interaction bonds J exposed to the spatially varying effective temperature $k_B T_{\text{eff}} / J = k_B T / J_i$. Then the quasiparticle localized on a certain bond feels the effective temperature and carries an energy corresponding to that of the bulk system at $k_B T_{\text{eff}}$. The trace of the product of the exponentials of these quasiparticle energy gives the partition function. The constituent of this product in a unit of the localized wave packet gives the local partition function, carrying an energy typical of that location. The system thus becomes a canonical ensemble of wave-packet states representing the thermal equilibrium at temperature $k_B T_{\text{eff}}$. We showed that this picture is valid by numerically evaluating the bond energy exactly for a finite-size L. Its deviation from the exact value in the thermodynamic limit is suppressed to less than 10^{-3}.

A practical advantage of using the SSD is that it generates a massive number ($L/2$) of data points with different $k_B T_{\text{eff}}$ by a single calculation at fixed $k_B T$. Therefore, we can perform Monte Carlo simulations on a large system and obtain a wide profile of the energy and the specific heat within sufficient accuracy with a low numerical cost. The SSD error is found to scale roughly with $1/\sqrt{L}$. When combined with the Gaussian kernel regression, the accuracy improves beyond the SSD error. The applications of the SSD to the MC simulations are very promising.

ACKNOWLEDGMENTS

[1] A. Gendiar, R. Krcmar, and T. Nishino, Prog. Theor. Phys. **122**, 953 (2009); **123**, 393 (2010).

[2] A. Gendiar, M. Daniska, Y. Lee, and T. Nishino, Phys. Rev. A **83**, 052118 (2011).

[3] N. Shibata and C. Hotta, Phys. Rev. B **84**, 115116 (2011).

[4] T. Hikihara and T. Nishino, Phys. Rev. B **83**, 060414(R) (2011).

[5] H. Katsura, J. Phys. A: Math. Theor. **44**, 252001 (2011).

[6] H. Katsura, J. Phys. A: Math. Theor. **45**, 115003 (2012).

[7] X. Wen, S. Ryu, and A. W. W. Ludwig, Phys. Rev. B **93**, 235119 (2016).

[8] K. Okunishi, Prog. Theor. Exp. Phys. (2016) 063A02.

[9] S. Tamura and H. Katsura, Prog. Theor. Exp. Phys. **2017**, 113A01 (2017).

[10] N. Ishibashi and T. Tada, J. Phys. A: Math. Theor. **48**, 315402 (2015).

[11] I. Kishimoto, T. Kitade, and T. Takahashi, Prog. Theor. Exp. Phys. **2018**, 123B04 (2018).

[12] X. Liu and T. Tada, Prog. Theor. Exp. Phys. **2020**, 061B01 (2020).

[13] R. Fan, Y. Gu, A. Vishwanath, and X. Wen, Phys. Rev. X **10**, 031036 (2020).

[14] B. Lapierre, K. Choo, A. Tiwari, C. Tauber, T. Neupert, and R. Chitra, Phys. Rev. Research **2**, 033461 (2020).

[15] D. S. Ageev, A. A. Bagrov, and A. A. Iliasov, Phys. Rev. B **103**, L100302 (2021).

[16] X. Wen, R. Fan, A. Vishwanath, and Y. Gu, Phys. Rev. Research **3**, 023044 (2021).

[17] R. Fan, Y. Gu, A. Vishwanath, and X. Wen, SciPost Phys. **10**, 049 (2021).

[18] C. Hotta and N. Shibata, Phys. Rev. B **86**, 041108(R) (2012).

[19] K. Okunishi and T. Nishino, Phys. Rev. B **82**, 144409 (2010).

[20] K. G. Wilson, Rev. Mod. Phys. **47**, 773 (1975).

[21] I. Maruyama, H. Katsura, and T. Hikihara, Phys. Rev. B **84**, 165132 (2011).

[22] C. Hotta, S. Nishimoto, and N. Shibata, Phys. Rev. B **87**, 115128 (2013).

[23] L. Onsager, Phys. Rev. **65**, 117 (1944).

[24] A. W. Sandvik, Phys. Rev. B **85**, 134407 (2012).

[25] B. Kaufman, Phys. Rev. **76**, 1232 (1949).

[26] M. Kac and J. C. Ward, Phys. Rev. **88**, 1332 (1952).

[27] P. B. Potts and J. C. Ward, Prog. Theor. Phys. **13**, 38 (1955).

[28] E. W. Montroll, P. B. Potts, and J. C. Ward, J. Math. Phys. **4**, 308 (1963).

[29] H. A. Kramers and G. H. Wannier, Phys. Rev. **60**, 252 (1941).

[30] H. A. Kramers and G. H. Wannier, Phys. Rev. **60**, 263 (1941).

[31] A. E. Ferdinand and M. E. Fisher, Phys. Rev. **185**, 832 (1969).

[32] T. D. Schultz, D. C. Mattis, and E. H. Lieb, Rev. Mod. Phys. **36**, 856 (1964).

[33] I. Klich, arXiv:cond-mat/0209642.

[34] See, e.g., Y. A. Bakhturin, in *Encyclopaedia of Mathematics*, edited by M. Hazewinkel (Kluwer Academic, Dordrecht, 2002).

[35] C. Hotta and K. Asano, Phys. Rev. B **98**, 140405(R) (2018).

[36] K. Harada, Phys. Rev. E **84**, 056704 (2011).

[37] T. Nakamura, Phys. Rev. E **93**, 011301(R) (2016).

[38] T. Nakamura, Sci. Rep. **10**, 14201 (2020).